COSMOS, Vol. 7, No. 1 (2011) 43–63

DOI: 10.1142/S0219607711000699

World Scientific
www.worldscientific.com

OPTICAL METAMATERIALS AND SUPER-RESOLUTION IMAGING

EUNICE S. P. LEONG, HONG LIU, YAN JUN LIU and JINGHUA TENG*
Institute of Materials Research and Engineering
*Agency for Science, Technology and Research (A*STAR), Singapore*
**jh-teng@imre.a-star.edu.sg*

Received 3 May 2011

1. Introduction

Metamaterials are specially designed periodic structures ($a \ll \lambda$) that give rise to extraordinary optical properties that no natural materials can possess. It can have extremely large refractive index or a negative refractive index over a frequency band. The refractive index, n, determines how light travels in a medium and is related to the permittivity, ε, and permeability, μ, by the relation $n = (\varepsilon\mu)^{1/2}$. It was first pointed out by Veselago that if $\varepsilon < 0$ and $\mu < 0$, then n becomes negative.[1] Nevertheless, there are no natural materials that possess negative permeability, though metals possess negative permittivity at subplasma frequency.[2] However it was Pendry's suggestion that negative refraction would make a perfect lens that drawn worldwide interests in this field.[3–5] Besides subwavelength diffraction limited imaging, metamaterials have also found applications in areas such as wideband directive antennas,[6] band-stop filters,[7] radar absorbers,[8] broadband phase shifters,[9] cloaking[10,11] and far-field optical microscopy.[12,13] These can be achieved by engineering the propagation of light in the structure. This list of potential applications is non-exhaustive as more concentrated efforts are currently ongoing all over the world to design new structures and improve on old ones. The beauty of using metamaterial structures in devices is that the design can be made much smaller with improved performances, or at least comparable performances with conventionally established techniques.

Ernest Abbe (1840–1905), a Germany physicist, discovered the resolution limit of optical microscope and described it with a well-known formula given by $d = \lambda/NA$, where d is the minimum distance between two objects to be resolved by an illumination system of a light wavelength of λ and an objective lens of numerical aperture NA.[14,15] The resolution limit of the conventional optical microscope is physically constrained by diffraction. It lasted for more than a century and a lot of research efforts have been put in overcoming it. It was not only until 2000, when Pendry proposed an idea termed as "perfect lens" — a thin slab of flat negative refractive index material — that was theoretically able to make perfect images without any deterioration nor information loss.[3] The scattering light from an object consists of propagating waves carrying large feature information while evanescent waves carrying fine feature (subwavelength) information. The evanescent waves deteriorate exponentially when traveling in any positive refractive index medium and cannot be recovered by the conventional optical lenses of positive index

materials, which is therefore accountable for the diffraction-limited images. Superior to conventional lenses, the "perfect lens" theoretically is able to make perfect images by enhancing evanescent waves passing through its negative index materials. The image was created in either near field or far field by recovering a combination of evanescent and propagating waves in image plane without any deterioration nor information loss. Pendry's theoretical proposal paved a way for further study and development of optical imaging beyond the diffraction limit. However, the electric and magnetic field are decoupled at subwavelength regime, which means either negative ε or negative μ is applicable for practice. Fang *et al.* conceived it and first experimentally demonstrated a superlens taking in material loss and other practical imperfections to account for differentiation from perfect lens, by which subwavelength imaging was successfully achieved in near field at UV region in 2005.[16] To get far field real-time super-resolution imaging, hyperlens is a promising technique to project and magnify subdiffraction limit image in far field.[17,18] Its unique design with employment of the multilayered cylindrical metamaterials requires relatively complex fabrication process to achieve the far field super-resolution imaging.

In this article, we present a review on the development of optical metamaterials and the use of plasmonic metamaterials for subdiffraction limit or super-resolution imaging. We will discuss about the fundamental and the recent achievements as well as look for its research trends in this rapidly growing field for emerging applications particularly in bio imaging and lithography. This article will be concluded with a brief overview of the research activities in A*STAR on metamaterials and superlens.

2. Development of Metamaterial Structures Towards Optical Frequencies

Most pioneer works on metamaterials were in the microwave range and studies were made to design structures to give electric and magnetic metamaterials. In general, plasmons in bulk metals occur in the optical regime and usually their permittivity is negative for frequencies between the damping and plasma frequencies of metals.[19] However, in the lower frequency range, the dielectric function of metal is imaginary. Nevertheless, Sir John Pendry pointed out that negative permittivity can be made possible at low frequency by structuring metals to reduce their plasma frequency.[19–21] This was later experimentally verified by Hibbins *et al.*[22] Pendry *et al.* then continue to show theoretically that by having a rolled metal sheet with gaps between each wound, negative permeability can be found. With that, they simplified the design to the double splitring resonators (SRRs) which shows negative permeability in the microwave range.[23] Based on these designs, Smith *et al.* demonstrated the first metamaterial structure that consists of metallic double SRRs and wire.[24,25] The schematic of the evolution of magnetic structure from rolled metal sheet to SRR with wire is shown in Fig. 1.

The SRR acts as an LC resonator whereby a current is induced when an external magnetic field

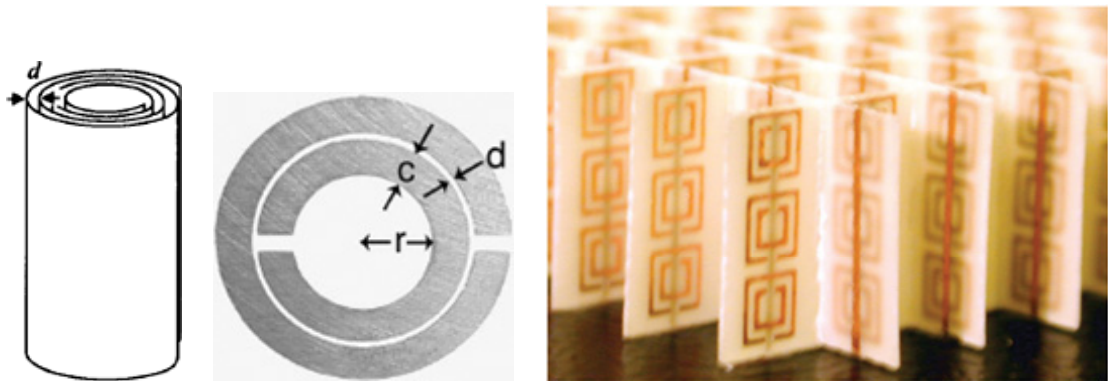

(a) (b) (c)

Fig. 1. (a) Schematic of the first proposed magnetic structure by Pendry (obtained from Ref. 23) which is simplified to the (b) SRR structure (illustration obtained from Ref. 24) (c) Experiment of the first negative index metamaterial which consists of continuous wire and SRR structure (obtained from Ref. 25).

with varying flux is normal to a metal loop, according to Faraday's law of induction. By Lenz's law, a magnetic field which opposes the change in induced current is generated. Due to the gap in the SRR, charges are stored as capacitance. This retards the opposing field at frequencies above resonance, thus giving rise to negative permeability. The negative permittivity is provided by the wire and this combination results in both negative permittivity and negative permeability and allows a pass-band as opposed to a dip for SRR alone in the transmission spectrum.[24,25] The later experimental verification that negative refraction does occur in such structures[26] intrigued more in-depth studies to design negative index materials to operate in THz and mid-IR regime.[27–29] To push the operating regime to the higher frequency range, the double SRR is simplified to a single split-ring design with much smaller dimensions and is demonstrated to operate at 100 THz.[30] In principle, the SRR operates below the plasma frequency of metal and the resonance frequency is inversely proportional to the size of the structure. As such, the u-shaped structure is designed as a simpler version of the SRR, which gives stronger resonance and at shorter wavelength at 1.5 μm.[31,32] However, there seems to be a limit to how small the structure can be scaled down due to the finite electron density in real metals, skin depth of metal and the consideration of interband transitions in metals at optical frequencies[33]. Moreover, such a structure can only provide negative permeability. Figure 2 shows how the SRR is simplified to the u-shape and cut-wire pair structure.

An alternative to the metallic split-ring or u-shaped structure is to create voids in metal/dielectric/metal (MDM) films. It is first demonstrated experimentally that negative index occurs in such a structure at 1.5 μm, and this structure has been coined as the fishnet structure.[34] In the direction parallel to the magnetic field, the magnetic field interacts with the MDM region and the induced current flows between the top and bottom metal films which form the inductor. Due to the presence of void, a closed loop flow of the induced current is not possible and a capacitance is built up between the metal films. As such, negative permeability can occur. On the other hand, the metallic region in the electric field direction forms negative permittivity. The idea is explained and illustrated in Ref. 35 and shown in Fig. 3. This seems to be a promising structure to produce double negative index in the optical regime and there have been several studies on such a structure to scale down to shorter resonance wavelength. This is done mainly by changing the type of metal, the dielectric, pitch and line width of metal grating in both electric and magnetic field directions, and thickness of the MDM structure and shape of void.[36–42]

Besides pushing metamaterials to operate in optical frequency, it is necessary to ensure that these structures perform well, with a quality indicator given by the figure of merit FoM ($-n'/n''$). It is also important to ensure there is impedance matching such that there is minimal reflection to degrade the performance.[43] Several theoretical and experimental studies have been concentrated on the design-related loss in the fishnet structure based on the type of voids, thickness of metal and structure design.[44–49] Practical use of metamaterials is limited by its narrow band of response and high loss. Hence, to tackle the issue of narrow band of response, metamaterials structure involving varying pitches,[50] displacement of layers in the x, y plane,[51] spatial arrangement of the structures in the case of sterometamaterials[52] or incorporation of tunable materials such as liquid crystals have been reported.[53–55] Their schematics are shown in Fig. 4. Adding gain material into metamaterial structure is one possible route to reduce loss. This is proposed by having a gain medium between two fishnet structures,[56] by embedding the fishnet structure in Rhodamine 800 dye molecules,[57] or by submerging metamaterial

Fig. 2. An effort to push the magnetic resonance to shorter wavelength region by transforming the SRR structure to u-shape to cut-wire pair (obtained from Ref. 33).

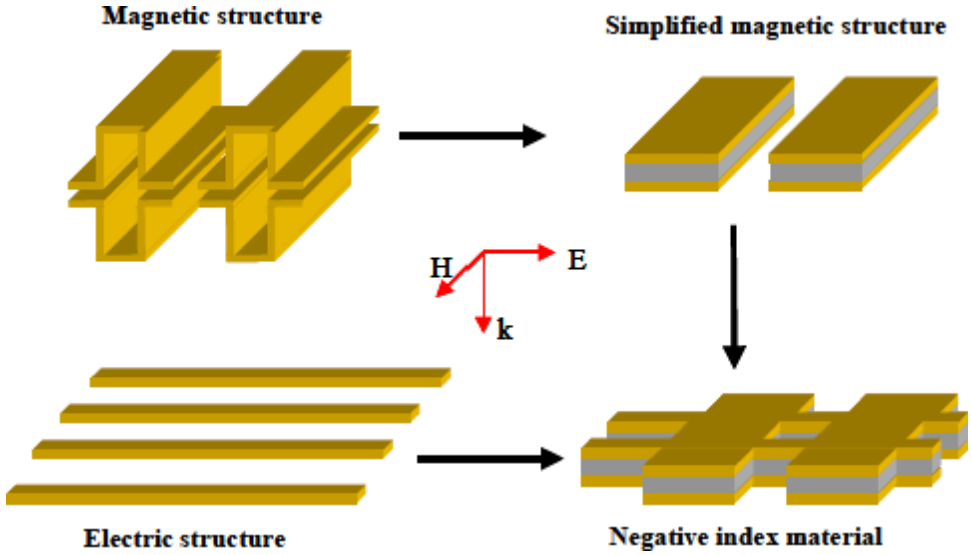

Fig. 3. Schematic showing how magnetic and electric structures are combined and simplified to form a double negative fishnet structure (obtained from Ref. 35).

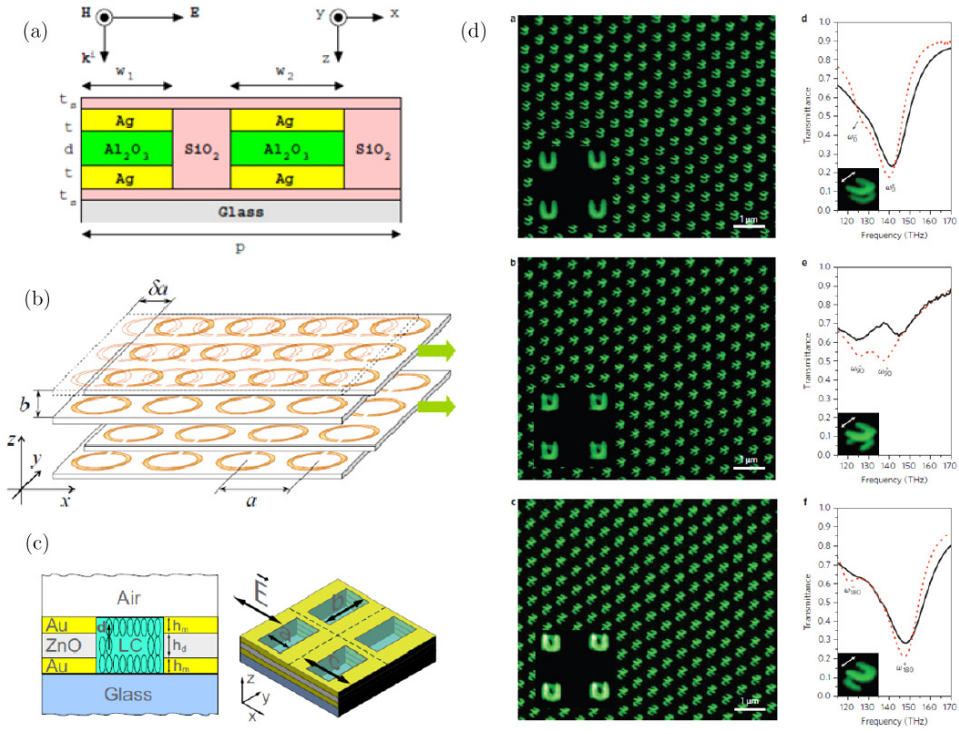

Fig. 4. Ways to combat the narrow band response of negative index: (a) Metamaterial structure with designs with varying pitch (obtained from Ref. 50), (b) Stacking of structure with x, y displacement (obtained from Ref. 51) (c) Incorporating liquid crystals (obtained from Ref. 53) and (d) Different orientation of structure for each stack (obtained from Ref. 52).

structure in active gain medium, as shown in Figs. 5(a) and 5(b).[58,59] For superlens application, incorporating gain in superlens can theoretically not only reduce loss but also increase the resolution,[60] thus forming an important point for fabricating low-loss metamaterial. Recently, Shalaev *et al.* have demonstrated a significant improvement in FoM through adding dye as a replacement of the alumina dielectric layer in the fishnet structure. The illustration of the fabrication of such structure is shown in

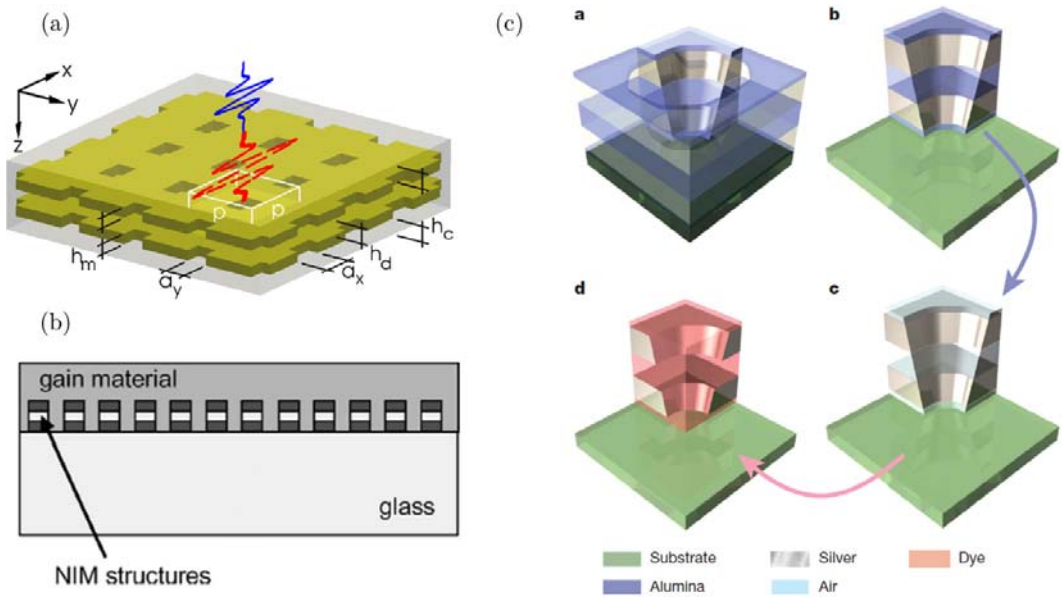

Fig. 5. Incorporating of gain material by immersing the (a) fishnet (obtained from Ref. 57) or (b) NIM structures in gain medium (obtained Ref. 59). (c) Schematic of fabrication process of replacing the dielectric layer by laser dye (obtained from Ref. 61).

Ref. 61 and Fig. 5(c). So far the structures discussed are of one-layer design. It is believed that with multilayer stacks, this will lead to improved transmission and reduced loss.[62] Nevertheless, the main issue of multilayer stacks lies in its fabrication. Three-functional layer has been realized by standard e-beam lithography and lift-off process.[63] Nevertheless, for much smaller structure where the resist cannot be too thick, the lift-off process can get more tedious for multilayer film evaporation.[64] One common way is to fabricate the first metal structured layer via lift-off or etching process, followed by planarization with dielectric or polymer and patterning of the second metal layer. The process is repeated till the desired number of layers is achieved.[65–67] Another promising way to make nanostructured multilayer stack is by focused beam milling.[68,69] In-depth reviews on the metamaterial structure evolution to operate in optical regime and its fabrication can be found in Refs. 64 and 70–72.

3. Superlens

In 2000, Pendry proposed that if there exists a lens of thickness d_2 with refractive index of -1 and located at distance d_1 from a light source, light will focus at $z = d_2 - d_1$ as shown in Fig. 6(a).[3,73] In the ideal case where $\varepsilon = \mu = -1$, the refractive index is negative

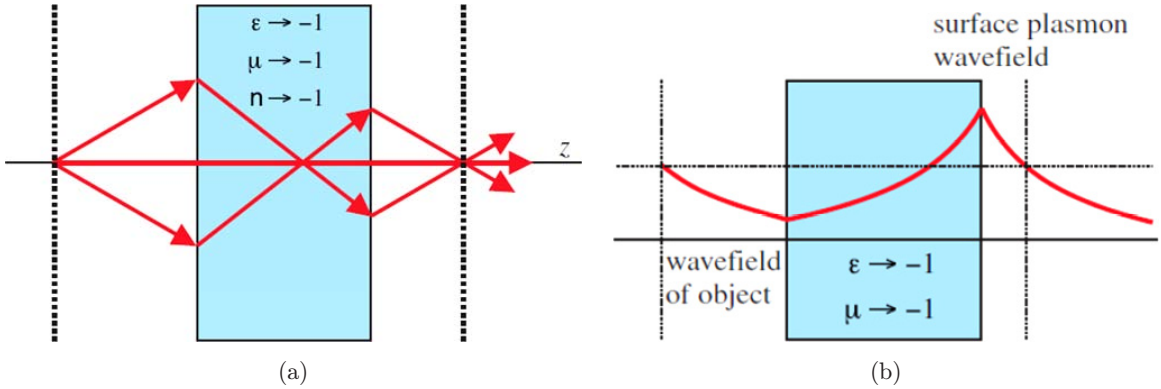

Fig. 6. (a) Light passes through a slab of refractive index -1 will focus instead of diverge as in the case of positive index medium. (b) Evanescent waves decay in air, is amplified at the metal–dielectric interface due to surface plasmons and is restored at the image point to preserve resolution of image (obtained from Ref. 73).

and the impedance $Z = (\mu\mu_0/\varepsilon\varepsilon_0)^{1/2} > 0$. Thus there is perfect match to free space with no reflections at the interface. In addition, the evanescent waves are amplified during the process and contribute to the resolution of the image (i.e. Fig. 6(b)). It was further proposed that using *p*-polarized light, only the condition $\varepsilon = -1$ is necessary, provided that the slab is thin and much smaller than wavelength of light.[3,74]

Based on this idea, the metamaterial superlens experiment was successfully demonstrated in 2005 by Fang *et al.* at 365 nm wavelength as mention above. As shown in Fig. 7(a), it utilized a thin slab of 35 nm silver as the superlens to be able to resolve 60 nm half-pitch grating structures recorded in photoresist, which is about one sixth of illumination wavelength of 365 nm. 60 nm half-pitch gratings were inscribed onto a 50 nm-thick chrome deposited on quartz substrate. It was then planarized with a 40 nm-thick layer of PMMA to provide a spacer between object and superlens. A 35 nm-thick silver layer was evaporated onto the spacer followed by coating with a 120 nm-thick negative photoresist for image recording at near field.

The substrate was then flood-exposed at 365 nm and developed. Thus, the near field optical imaging was converted into the surface morphology of the developed negative photoresist, which was mapped by atomic force microscopy (AFM) as shown in Fig. 7(b). In comparison, a control sample prepared by replacing the silver layer with a PMMA layer of the same thickness was not able to resolve the 60 nm half-pitch object and its corresponding image shown in Fig. 7(c). This work laid a foundation for consequential studies of superlens at optical frequency, which could result in significant impacts for applications such as lithography for the semiconductor industry. Another research group also presented silver superlens effect using similar scheme almost in the same year.[75] After that, similar designs and characterizations methods have been commonly applied for further optimization and development at the wavelength from near to deep UV range.[76–79] So far, the finest resolvable features imaged by superlens are the 30 nm half-pitch nanoimprinted lines using a Ge wetting layer to get an ultra-smooth silver superlens.[79] Figure 8(a) schematically shows the design of this 15 nm thick silver superlens evaporated on a seed layer of 1 nm Ge to achieve a surface roughness at about 0.8 nm. The image shown in Fig. 8(b) indicated that the smooth Ag superlens had minimized the subwavelength information loss due to scattering, in order to realize a high image resolution of about $\lambda/12$ at 380 nm wavelength.

Superlens effect has also been demonstrated at other frequencies. A low loss SiC superlens with an image resolution $\lambda/20$ in terms of wavelength was demonstrated at mid-infrared frequency ($\lambda \approx 11\ \mu$m) through direct mapping with NSOM,[80] as shown in Fig. 9. The superlens was a 440 nm single crystal SiC film with both sides coated with 220 nm SiO_2 films. 60 nm thick Au film with holes of diameters from 540 nm to 1200 nm are the objects to be imaged. The recorded NSOM images of amplitude and phase contrast were able to sufficiently resolve the $\lambda/20$-sized objects.

The above superlens is able to make subdiffraction-limit imaging at near field or the vicinity of superlens

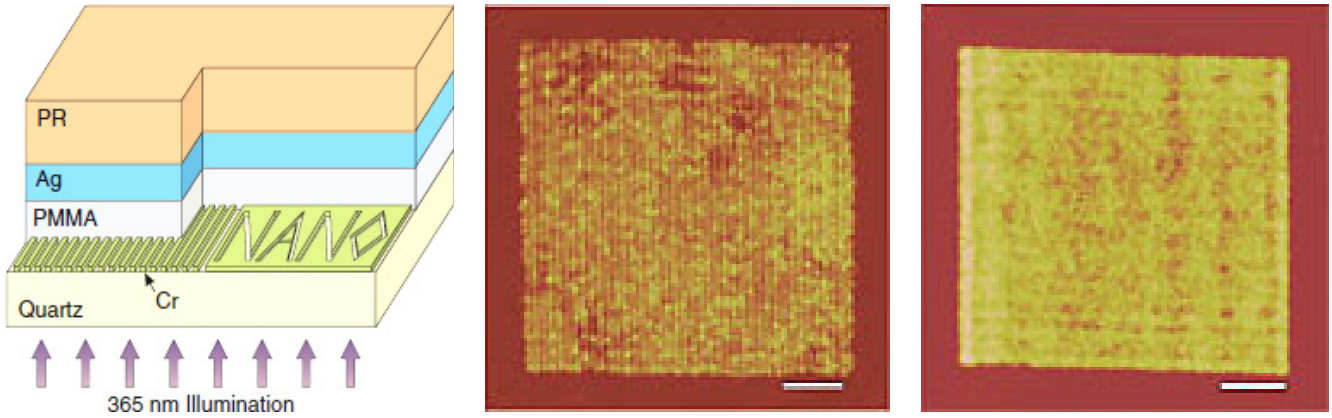

(a) (b) (c)

Fig. 7. The optical superlens demonstrated by Fang *et al.* at 365 nm. (a) The schematic view of experiment; (b) AFM image of the developed photoresist image of 60 nm half-pitch grating object (scale bar: 1 μm); (c) Control image without superlens. [Figure obtained from Ref. 16].

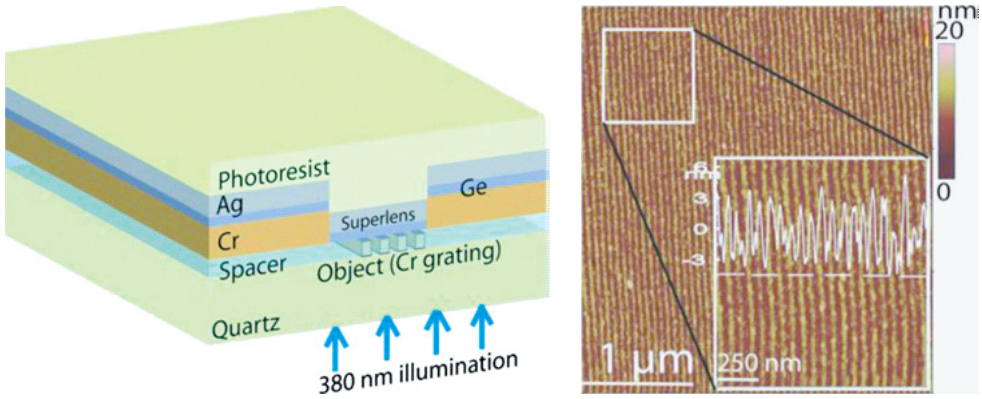

(a) (b)

Fig. 8. The ultra-smooth silver superlens deposited on a seed layer of Ge with nanoimprinted 30 nm half-pitch Cr gratings on quartz substrate. (a) Schematic view of the design operating at 380 nm wavelength, (b) The subdiffraction-limit optical imaging achieved by AFM scanning the developed photoresist over an area of 3×3 μm^2 [figure taken from Ref. 79].

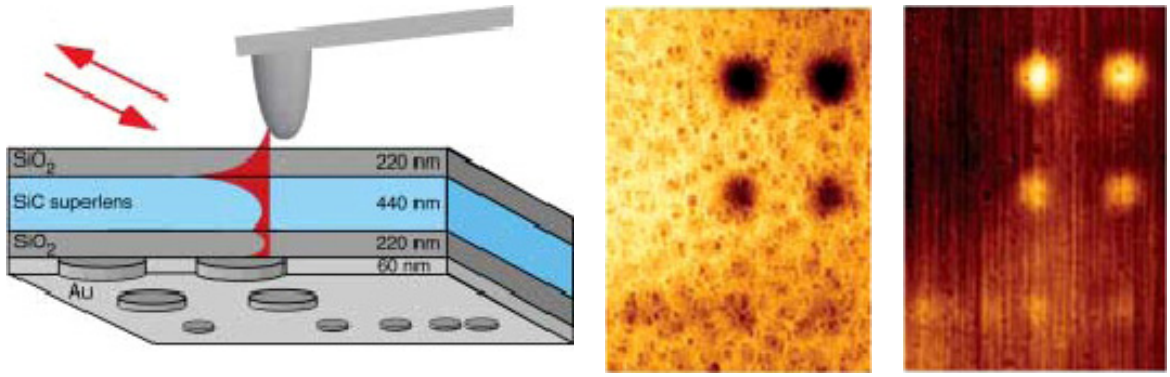

(a) (b) (c)

Fig. 9. A 880 nm thick SiC superlens structure scanned imaging at mid-infrared frequency ($\lambda \approx 11$ μm): (a) Experimental setup, (b) Superlensing amplitude image by NSOM, (c) Phase contrast image. [figure obtained from Ref. 80].

surface. In practical usage a far field imaging could give the chance to observe nanometer scale features directly. Therefore, scientists have been motivated and proposed a far field superlens made of thin flat silver plus periodic corrugations.[81–83] The far field superlens significantly enhanced the evanescent waves of the object and converted them into propagating waves by a coupling element of periodic gratings as shown in Fig. 10. The design of this far field superlens is detailed in Fig. 10(a). Its detection setup is schematically shown in Fig. 10(b) with an incident light of wavelength 377 nm illuminating from the substrate side. A pair of 40 nm-thick Cr slits with a width of 50 nm and space of 70 nm is patterned by focused ion beam on quartz substrate and its SEM picture is shown in Fig. 10(c). Figure 10(d) shows the diffraction-limited image by a conventional microscope, which is not able to resolve the two nanowires due to the diffraction limitation as expected. In comparison, the evanescent waves scattered from the object are significantly enhanced by surface plasmon excitation followed by transforming into propagation waves in the far field with *p*-polarized illumination. Subsequently the evanescent information with *p*-polarized light and propagating information under *s*-polarized light was coupled by this far field superlens to make such a pair of 50 nm-wide lines clearly resolvable in the far field as shown in Fig. 10(e). Superior to those point-by-point scanning techniques, far field superlens exhibit several advantages such as high throughput and real-time imaging, which enables it as a promising tool for the application in bio-imaging and brings us closer to the ultimate goal of a nanoscope.

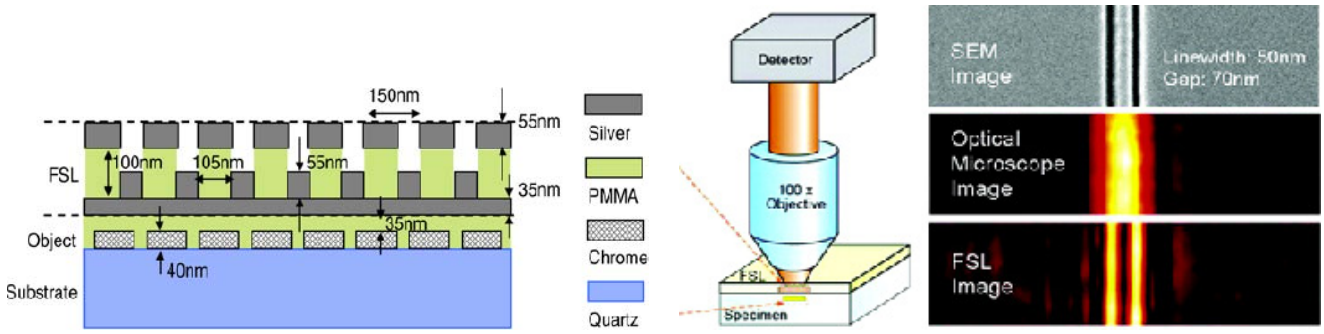

(a) (b)

Fig. 10. (a) Detailed design of the far field superlens structure. (b) Experimental setup for the detection of far field imaging. (c) SEM picture of a pair of object nanowires with 50 nm width separated by 70 nm gap. (d) Diffraction-limited image obtained by conventional optical microscope. (e) Far field superlens imaging with both p and s polarizations to resolve the subwavelength object by surface plasmon enhancement [Figures obtained from Ref. 81–83].

In the above cases of a thin silver slab acting as the superlens, the system is susceptible to high absorption loss and the transmission tends to be low. Pendry *et al.* initiated using a multilayer stack consisting of thin ($\sim 5-10$ nm) metallic and high dielectric constant dielectric films to image in the near field to minimize the absorption effect.[72,84] An advantage is that the multilayer films possess anisotropic properties and allow light to be guided with little diffraction. Thus at zero frequency, the image is formed directly from the object.[72,85] However such thin films are difficult to fabricate as they tend to be semi-continuous. Therefore Scalora *et al.* designed a metal–dielectric photonic band-gap structure with dielectric thickness to be $\lambda/4 - \lambda/2$. The metal films form a cavity and light tunnel through the layers at wavelength λ.[85] In their example, the metal, Ag, is 32 nm thick and the dielectric of $n = 4$ is 21 nm thick. The resonance wavelength is around 400 nm and this can be altered by changing the thickness of the films and refractive index of the dielectric. The tunability and enhanced resolution of a metal–dielectric lens design compared to a single slab make it a more attractive way to achieve subwavelength imaging. Therefore there have been several efforts to study theoretically the design of metal–dielectric lens structure[86,87] and experimentally to form smooth MDM structures.[88–90]

4. Hyperlens

Hyperlens is similar to the metal–dielectric stack lens design except that it offers extra feature of magnification. The term "hyperlens" comes from the use of a metamaterial with a hyperbolic dispersion relation — the root governing the ability of the hyperlens to resolve images beyond the diffraction limit.[91] Considering a cylindrical coordinate system (r, φ, z) with no z-variation and an anisotropic permittivity, the dispersion relation of an electromagnetic wave can be written as

$$\frac{k_r^2}{\varepsilon_\varphi} + \frac{{k_\varphi}^2}{\varepsilon_r} = \frac{\omega^2}{c^2} \tag{1}$$

where k_r and k_φ are the wave vectors and ε_r and ε_φ are the electric permittivities along the $\vec{r}$ and $\vec{\varphi}$ directions, respectively; ω is the circular frequency and c is the velocity of light. For common dielectrics (i.e. materials which exhibit positive real permittivity), this equation is that of an ellipse. Thus, the total wave vector of an electromagnetic wave at a given frequency is bound to the perimeter of this ellipse, as shown by the short-dashed curve in Fig. 11(a). This condition on the magnitude of the wave vector places an intrinsic limit on the spatial frequencies that a traditional lens may resolve. Assuming $\varepsilon_\varphi > 0$ and $\varepsilon_r < 0$, a hyperbolic dispersion relation [solid curve in Fig. 11(a)] will be given by Eq. (1). At such a condition, the isofrequency curve of the k_r, k_φ plot becomes a hyperbola, thus yielding an unbound value of the magnitude of the wave vector. Therefore, it becomes possible that such a material system can be used to fabricate a lens capable of arbitrarily imaging high spatial frequencies, thus surpassing the diffraction limit. Due to the relatively unusual conditions of the permittivity components, metamaterials are the logical option to construct the hyperlens. It is worth noting that such metamaterials possessing dielectric

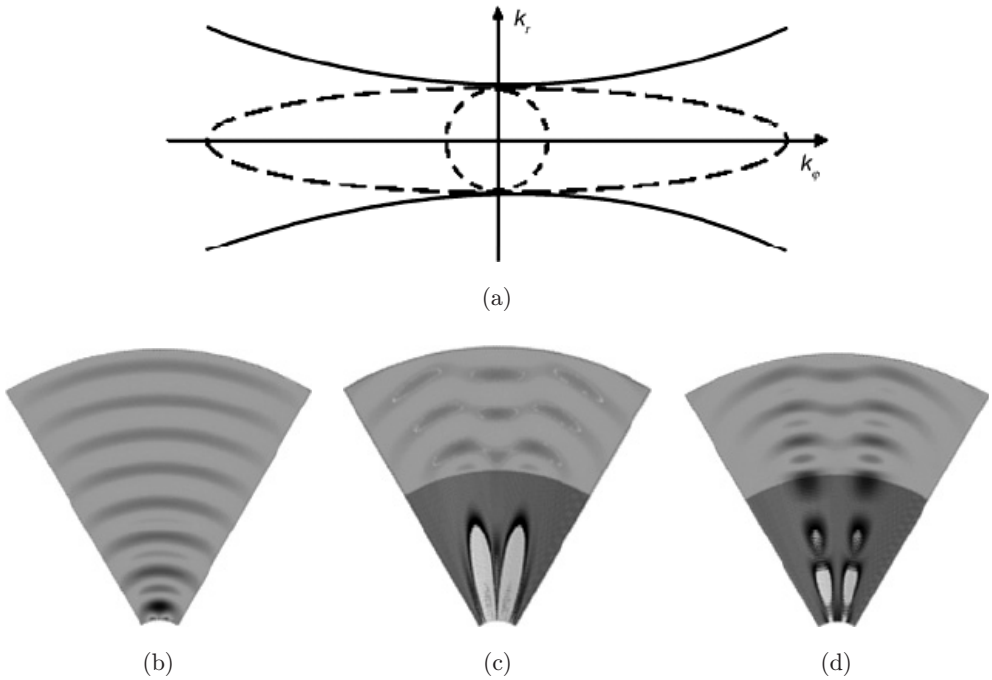

Fig. 11. (a) Isofrequency dispersion contours indicating circular ($\varepsilon\varphi = \varepsilon r > 0$), elliptical ($0 < \varepsilon\varphi \neq \varepsilon r > 0$), and hyperbolic ($\varepsilon\varphi > 0, \varepsilon r < 0$) behavior. (b)−(d) Simulated field distributions arising from two point sources spaced at a subwavelength distance. (b) Field plot showing that the two separate sources cannot be imaged under ordinary circumstances. (c) When placed at the input of the hyperlens (with a hyperbolic dispersion), however, information distinguishing the two point sources propagates to the far field. (d) When using a metamaterial that exhibits a highly eccentric elliptical dispersion, a similar super-resolution imaging is observed but with degraded image fidelity. (Figure obtained from Ref. 93.)

anisotropy of differing signs are now known as indefinite media.[92]

Figures 11(b)−11(d) shows the comparison of finite element method (FEM) simulations of the hyperlens design with an ordinary material and metamaterial. Figure 11(b) shows the optical field distribution in an ordinary material due to two point sources separated by a subwavelength distance; clearly, the image of two separate sources is irresolvable in the far field. By placing the two subwavelength-separated point sources in close proximity to the inner surface of the hyperlens, as shown in Fig. 11(c), the optical field distribution yields an image of the two sources in the far field. Ma *et al.* have also discussed that the hyperbolic dispersion may not be strictly necessary.[93] The purpose of the hyperbolic dispersion is to access large components of the tangential wave vector. However, the same access could be achieved based on high eccentricity elliptic dispersion (long-dashed curve in Fig. 11(a)). The corresponding field simulation is shown in Fig. 11(d); similar far field imaging of a subwavelength feature is realized although it is not as good as the hyperbolic case of Fig. 11(c).

Considering the fact that real materials exhibit a certain degree of loss, a design with cylindrical geometry was therefore proposed for the hyperlens. In this geometry, the compression of the φ-component of the wave vector transforms evanescent portions of the angular spectrum into resolvable information and the magnification at the output surface is given simply by the ratio of the radii at the two surfaces $r_{\text{outer}}/r_{\text{inner}}$.[90,93,94] The designed hyperlens may have strong anisotropy in the metamaterial permittivity, which could induce strong scattering and hence damage the imaging quality.[94] To avoid this, an impedance match between the hyperlens metamaterial with the medium it is immersed in needs consideration, to minimize the surface reflections.[95]

The first optical hyperlens was experimentally demonstrated using the conformal film deposition method on a half-cylindrical cavity on a quartz substrate.[96] It consisted of 16 pairs of layers composed of 35 nm-thick silver and 35 nm-thick alumina, above which a 50 nm-thick chromium layer was deposited to block the unwanted incident light, as shown in Fig. 12(a). A plane wave at the

wavelength of 365 nm was used to illuminate the subdiffraction limit objects milled on the chrome layer. The light scattered (evanescent wave) by the objects that possessed high transverse k-vectors could be collected by the hyperlens and continue to propagate outward along the radial direction. During the propagation, the high transverse k-vectors were compressed gradually, resulting in a magnified image of the subdiffraction-limited object on the outer boundary of the hyperlens. The k-vector of the image on the outer boundary was compressed small enough to propagate in the medium surrounding the outer boundary of hyperlens, so the image could continue to propagate and thus be detected with conventional optics in the far field. The first hyperlens demonstrated can directly resolve a pair of lines 35 nm wide, separated by 130 nm, in the far field under a conventional microscope, as showed in Fig. 12(b). Figure 12(c) showed the comparison of the images acquired without the hyperlens, in which the subdiffraction limited object cannot be resolved. Such a hyperlens can magnify arbitrary objects with subdiffraction-limited resolution because it can support the propagation of a very broad spectrum of wave vectors. Figure 12(d) is the proof that a clear image of the letters "ON" shows the fine features of the object.

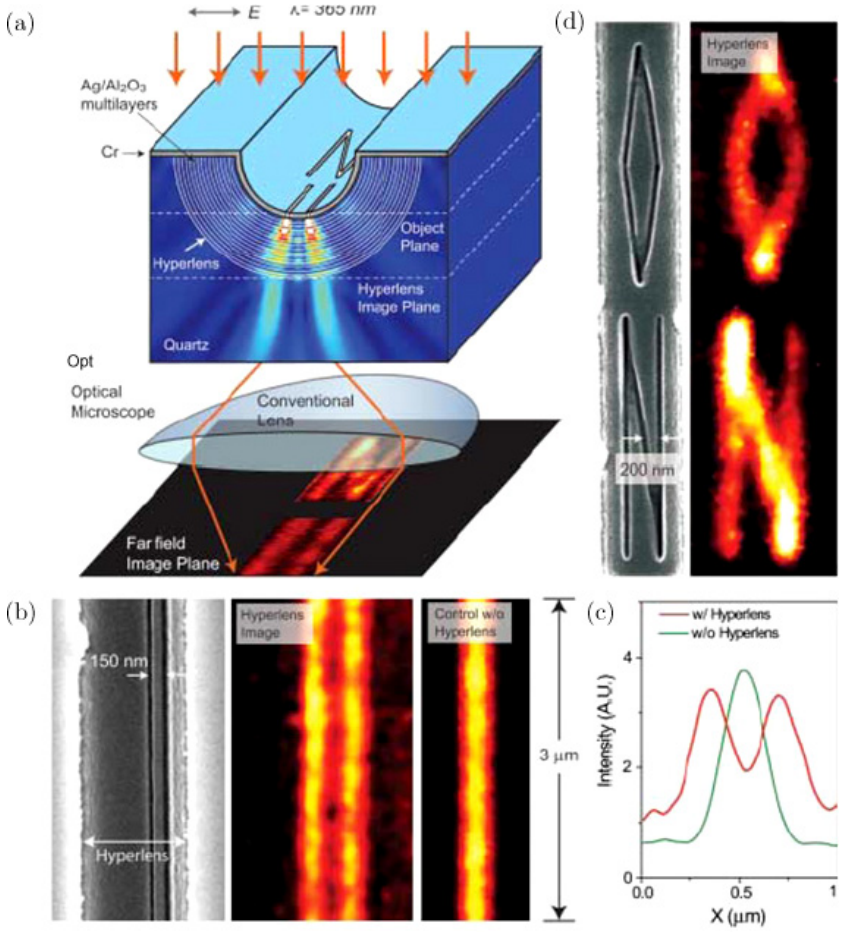

Fig. 12. Magnifying optical hyperlens. (a) Schematic of hyperlens and numerical simulation of imaging of subdiffraction-limited objects. (b) Hyperlens imaging of line pair object with line width of 35 nm and spacing of 150 nm. From left to right, scanning electron microscope image of the line pair object fabricated near the inner side of the hyperlens, magnified hyperlens image showing that the 150 nm-spaced line pair object can be clearly resolved, and the resulting diffraction-limited image from control experiment without the hyperlens. (c) The averaged cross section of hyperlens image of the line pair object with 150 nm spacing (red), and a diffraction-limited image obtained in the control experiment (green). A.U., arbitrary units. (d) An arbitrary object "ON" imaged with subdiffraction resolution. Line width of the object is about 40 nm. The hyperlens is made of 16 layers of Ag/Al_2O_3. (Figure obtained from Ref. 96.)

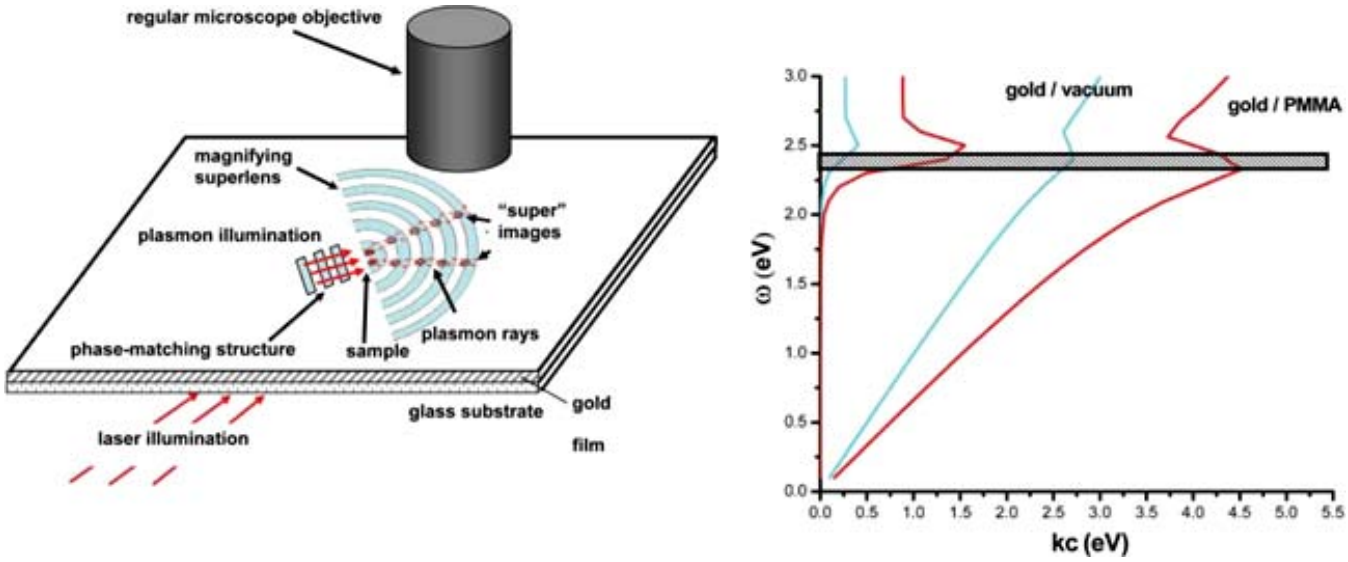

(a) (b)

Fig. 13. (a) Schematic of the magnifying superlens integrated into a conventional microscope. (b) Real and imaginary parts of the surface plasmon wave vector k at the gold−PMMA and gold−vacuum interfaces as a function of frequency. In the frequency range marked by the box, PMMA has negative refractive index as perceived by plasmons, whereas the gold−vacuum interface looks like a medium with positive refractive index. (Figure obtained from Ref. 97.)

Another type of cylindrical hyperlens is reported by Smolyaninov *et al.*[97] Figure 13(a) shows the schematic of the cylindrical magnifying hyperlens, which is based on the theoretical proposals of an optical hyperlens,[91] metamaterial crystal lens[92] and plasmon-assisted microscopy technique.[98] The plasmons generated by the phase-matching structure illuminate the sample positioned near the center of the superlens. The lateral distance between the images produced by the alternating layers of materials with positive and negative refractive index grows with distance along the radius. The magnified images are viewed by a regular microscope. This magnifying hyperlens consists of concentric alternate PMMA and vacuum rings on a gold film. The SPP dispersion for the gold−vacuum and gold−PMMA interfaces in the frequency range is marked by the box in Fig. 13(b). PMMA has negative refractive index $n_{\mathrm{PMMA}} < 0$ as perceived by plasmons (the group velocity is opposite to the phase velocity). The width of the PMMA rings d_{PMMA} is chosen so that $n_{\mathrm{vac}} d_{\mathrm{vac}} = -n_{\mathrm{PMMA}} d_{\mathrm{PMMA}}$, where d_{vac} is the width of the gold−vacuum portions of the interface and n_{vac} is the refractive index of vacuum. At this condition, all the rays in the superlens tend to propagate along the radial direction. Such a magnifying superlens can directly resolve at least 70 nm, or $\sim l/7\lambda$ at the wavelength of 495 nm.

For hyperlens imaging, it would be beneficial to make the working wavelength cover the entire visible light band, and thus enable a broad range of applications, such as the study of live cells and molecules. Smith *et al.* have theoretically investigated the metamaterial optical hyperlens for this purpose.[99,100] Two different material systems, Al_2O_3/Ag and TiO_2/Ag, were investigated for the visible band for oxides: metal volume ratios ranging from 0 to 6. Figure 14 clearly shows that the material combination and wavelength can be used for designing a visible hyperlens.

Very recently, Rho *et al.* reported the spherical hyperlens with resolution beyond the diffraction limit in two lateral dimensions at a visible wavelength.[101] The design is shown in Fig. 15. The spherical hyperlens is arranged in hemisphere geometry with alternating metallic and dielectric layers, as shown in Fig. 15(a) and a cross section drawing in Fig. 15(b). It consisted of nine pairs of layers composed of 30 nm-thick silver and 30 nm-thick titanium oxide, above which a 50 nm-thick chromium layer was deposited to block the unwanted incident light. The titanium oxide chosen here is to match the magnitudes of permittivities in the silver at

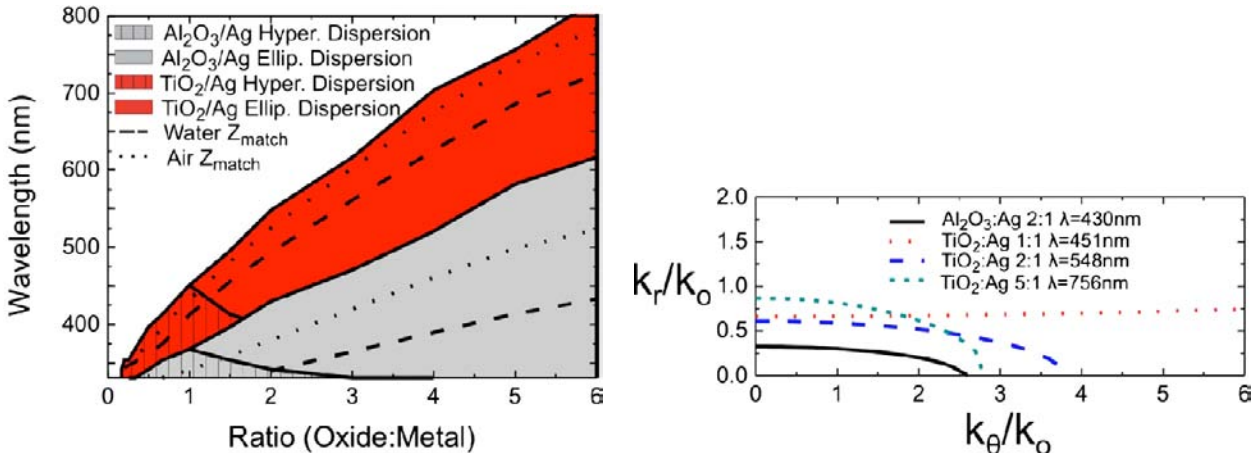

(a) (b)

Fig. 14. The anisotropic range of a hyperlens with different ratios of oxide to metal is presented (Al_2O_3/Ag plot overlaid on TiO_2/Ag plot). (a) The tunable hyperbolic dispersion range (solid color with bars) is defined to be where $\mathrm{Re}\{\varepsilon r\} < 0$ and $\mathrm{Re}\{\varepsilon\theta\} > 0$, given the criteria for the hyperlens effect and elliptical dispersion range (solid color), which is defined as $\mathrm{Re}\{\varepsilon r\} \gg \mathrm{Re}\{\varepsilon\theta\}$. The dotted lines are the wavelengths required for impedance matching (Zmatch) the given metamaterial lens with air, whereas the dashed are those required for matching with water, which result in a high transmission into the far field. (b) The dispersion relation for different material makeup is shown at different wavelengths in the visible spectrum. This illustrates the fact that the dispersion relation, whether hyperbolic or elliptical, is relatively flat, which results in high resolution of high order spatial information. (Figure obtained from Ref. 99.)

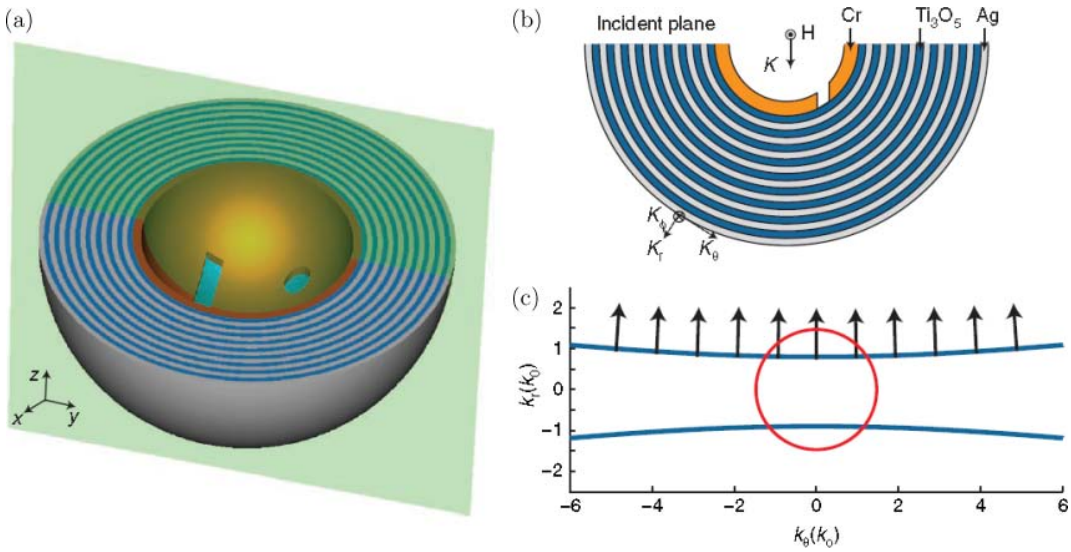

Fig. 15. Working principle of the spherical hyperlens. (a) Schematic of a spherical hyperlens comprised of nine pairs of silver and titanium oxide layers. (b) Cross section of the spherical hyperlens along the green incident plane. The object with subwavelength features is carved in a chromium layer atop the silver−titanium oxide multilayer (also shown in light blue in (a)). The transverse magnetic (TM) component of unpolarized light relative to the plane is labeled by K. (c) The isofrequency contour for the TM modes in the hyperlens compared with isotropic medium made of silicon oxide. The arrows, which are of unit length and on the ultraflat curve, show that all the k components (including those much larger than the wave vectors available in dielectrics) propagate along the same radial direction, indicating the lack of diffraction. (Figure obtained from Ref. 101.)

the operation frequency. At 410 nm, the titanium oxide has a dielectric constant of 5.83, whereas the permittivity of silver at this wavelength is $-4.99 + 0.22i$.[102] It was designed with flat hyperbolic dispersion that supports wave propagation with very large spatial frequency and yet same phase speed. A small positive ε_θ together with a large negative ε_r results in the propagation of a transverse

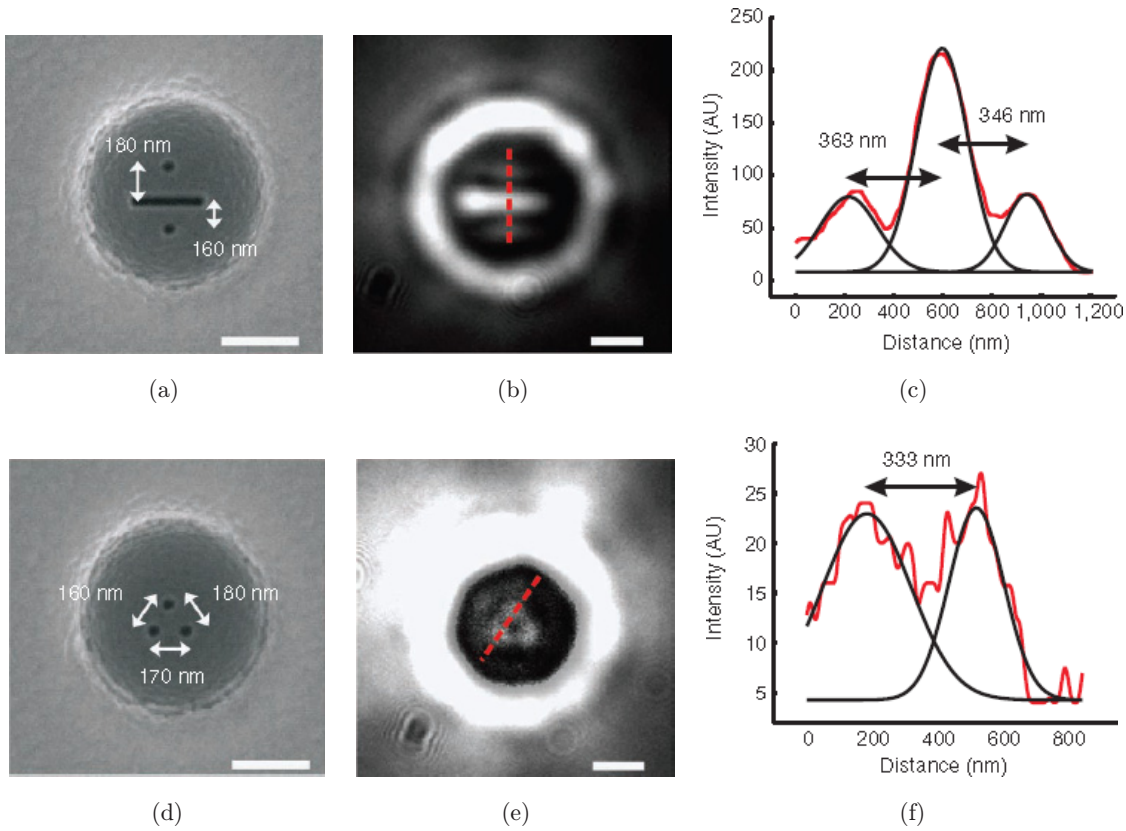

Fig. 16. Measurement with the magnifying hyperlens. (a) Scanning electron microscope (SEM) image of object 1: two 100 nm diameter dots separated by a 100 nm wide bar. The gap sizes are 180 and 160 nm. All scale bars shown in the figure are 500 nm. (b) Image of the object being magnified by the hyperlens. The subdiffraction-limited objects were clearly resolved by the spherical hyperlens. Along the red dashed line, a cross section is taken to calibrate the performance of the hyperlens. (c) Cross-sectional analysis showing separation by 363 and 346 nm, respectively, corresponding to 2.1 × magnification. (d) SEM image of object 2: three dots positioned triangularly with gaps of 180, 170 and 160 nm. (e) and (f) Image and cross section of the object along the red line after being magnified. (Figures obtained from Ref. 101.)

magnetic wave being governed by a flat hyperbolic isofrequency contour shown in Fig. 15(c), which allows the propagation of waves with much larger spatial frequencies than in natural media. This designed spherical hyperlens can resolve features down to 160 nm, much smaller than the diffraction limit at visible wavelengths, that is, 410 nm, as shown in Fig. 15.

The demonstration of hyperlenses has sparked tremendous research interest and applications. The hyperlenses have the capabilities to directly demonstrate subdiffraction limited resolution imaging in the far field, hence the time-consuming point-by-point scanning and image reconstruction can be avoided. Reciprocally, they can also be used for subdiffraction photolithography by recording the minified image of an object in the outer space far field into the photoresist. Therefore, hyperlenses are very promising in various areas for different applications, such as super-resolution imaging, nanophotolithography,[103] sensing and information storage.

5. Three-Dimensional Metamaterials for Imaging

Currently, the research on hyperlenses is still in the early stage and the proof-of-concept experiments only show promising but preliminary results. The performance of a hyperlens can be further boosted by optimization in terms of geometric designs, material losses and fabrication processes. The main limitation of the hyperlens imaging is that the object has to be placed very close to the inner surface of the hyperlens, which physically limits the imaging depth and field of view. In addition, the demonstrated hyperlenses so far can only achieve super-resolution in either one or two directions. For practical applications, it is highly desirable to achieve three-dimensional hyperlenses

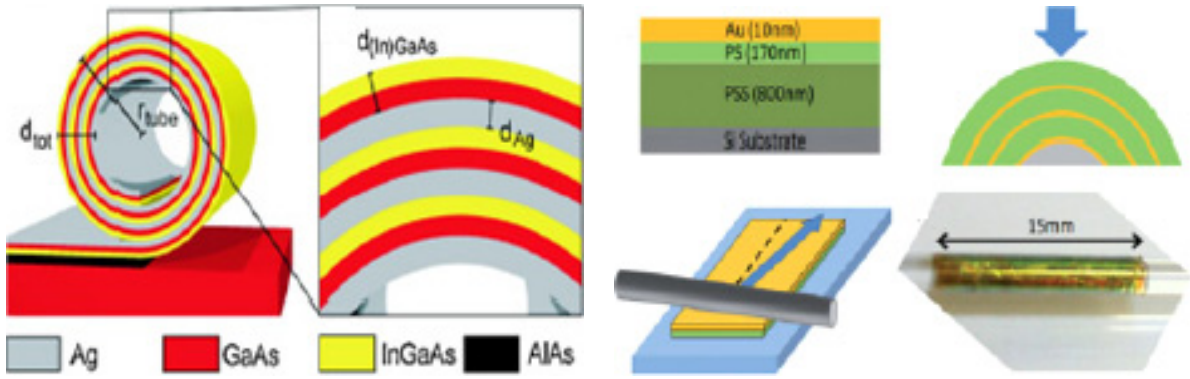

(a) (b)

Fig. 17. (a) The films are rolled up to minimize strain energy when AlAs sacrificial film is etched away. (Obtained from Ref. 104) (b) The films are rolled in a helical manner around a quartz rod when the PSS is dissolved. (Subfigure obtained from Ref. 105.)

with super-resolution in all directions. Therefore, there have also been intense efforts in fabricating isotropic negative index metamaterials in a hope to realize high resolution lenses.

One way to make three-dimensional structure is first to deposit the multilayer films and then roll them to form a tube. In the work by Mendach *et al.*,[104] they had an AlAs sacrificial layer below the strained InGaAs, GaAs and Ag multilayers. When the AlAs sacrificial layer is etched away, the metal–dielectric stack minimizes strain energy by rolling into a tube, as illustrated in Fig. 17(a). In a separate work by Gibbons *et al.*, they used a 0.8 μm layer of polystyrene sulfonic acid (PSS) film as a sacrificial layer on Si substrate. Au and polystyrene films are used as the metal–dielectric stack. When PSS is dissolved, the films are rolled around a cylindrical quartz rod in a helical manner, as shown in Fig. 17(b).[105]

On a different approach, Burckel *et al.* recently demonstrated the fabrication of three-dimensional metamaterial using self-aligned membrane projection lithography.[106,107] In their method, they first created an opening, and on top of the opening, there is a PMMA resist patterned membrane. The membrane acts as a shadow mask where metal films are deposited on the structure at various deposition angles. As such, the metamaterial structure is created on different sides of the opening beneath the membrane, as shown in Fig. 18.

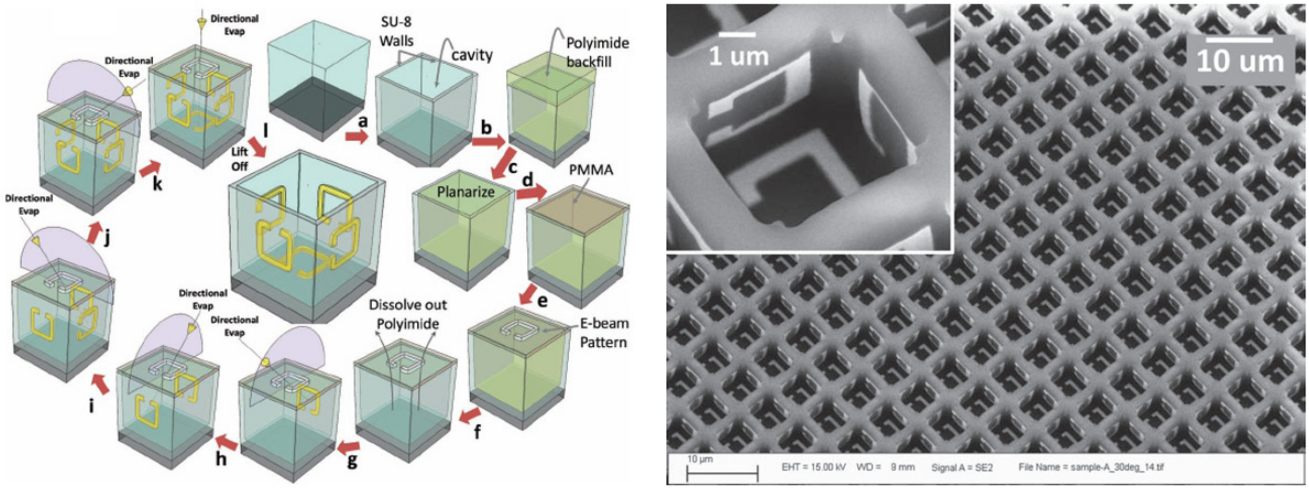

(a) (b)

Fig. 18. (a) Fabrication process for three-dimensional metamaterial fabrication and (b) SEM image of the fabricated structure. (Figure obtained from Ref. 106.)

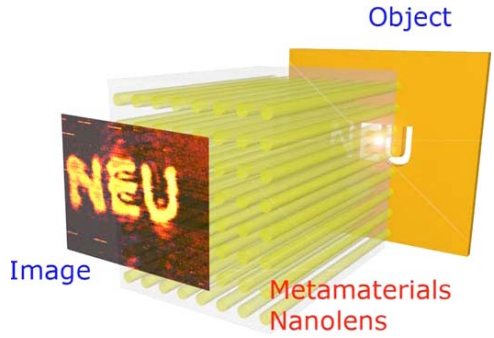

Fig. 19. Three-dimensional metamaterials nanolens enabled subwavelength imaging at 1550 nm. The nanolens employed high aspect-ratio Au nanowires grown in dielectric medium and the image was scanned by NSOM. [Figure obtained from Ref. 108.]

Another method for far field super-resolution imaging has been experimentally demonstrated recently by using aligned gold nanowires embedded in a porous alumina matrix to achieve a resolution of at least $\lambda/4$ at near-infrared wavelength (1550 nm).[108] The 10 μm-thick composite medium serving as three-dimensional metamaterials superlens enabled transferring both far field and near field information over a remarkable distance of more than 6λ, as shown in Fig. 19.

6. Metamaterials and Superlens Research in A*STAR

Foreseeing its enormous potential applications in industries like semiconductors, microelectronics, optics, green energy and biomedical engineering, the Agency for Science, Technology and Research (A*STAR) has started a Metamaterials Programme in 2010 to develop metamaterials and plasmonics science and technology and especially their industry applications. This program cuts across the local research organizations and draws on existing capabilities from both A*STAR and local universities, the Nanyang Technological University (NTU) and the National University of Singapore (NUS), to collaboratively work on this area. Superlens project is one of the projects under this program to develop the super-resolution imaging technology through innovations in structure design, materials engineering and two-dimensional/three-dimensional optical metamaterials fabrication to enhance the quality of super-resolution imaging. Some of the results are briefly introduced below.

Minimizing surface roughness of the metals and dielectrics is one of the most essential specifications to deliver subdiffraction-limit imaging. Rough surface leads to increasing scattering loss to demolish the subwavelength information carried by evanescent waves, which would be the major obstacle for superlens fabrication. Polymer-based dielectrics are naturally smooth after spin-coating with sub-nanometer roughness. Although the surface becomes rough after undergoing dry etching process to thin initial thickness down to a desirable value, a reflow process is effective enough to produce a smooth surface of a roughness comparable to its initial surface.[109,110] In contrast, silver films, which have been most frequently employed in superlens due to its intrinsic optical properties, exhibit rough surfaces of above 2 nm in terms of root mean square (rms) produced by conventional deposition methods such as sputtering, evaporation and electroplating, etc. Producing ultra-smooth silver films has been propelled by the increasing demand not only from the development of subdiffraction-limit imaging, but also nanoplasmonics and negative refractive index materials.

An effective method to produce ultrasmooth silver films by deposition on top of a thin seed layer of germanium has been reported.[111] A dramatic improvement of surface roughness to about 0.6 nm (rms) with a 15 nm Ag/2 nm Ge film has been achieved by electron beam evaporation. Liu *et al.* have also been motivated to find a seed layer material to be able to not only create an ultra-smooth Ag film, but also improve its surface plasmon resonance (SPR) for plasmonic and metamaterials applications. Both Ag/Ni and Ag/Ge films are investigated in terms of surface plasmon resonance through experimental and theoretical means, as well as compared with a pure Ag film.

Figure 20 shows the surface topographies of Ag/Ni films deposited on silicon and quartz respectively, and the surface plasmon resonance reflectivity curve at 632.8 nm wavelength. Both experimental and simulation results show that the Ag/Ni films exhibit an enhanced SPR over the pure Ag film with a narrower full width at half maximum. Ag films with a Ge seed layer have also been prepared under the same conditions. The surface roughness can be reduced to less than 0.7 nm, but narrowing of the SPR curve is not observed due to increased absorptive damping in the Ge seed layer. The results show that Ni acts as a growth layer of diminishing

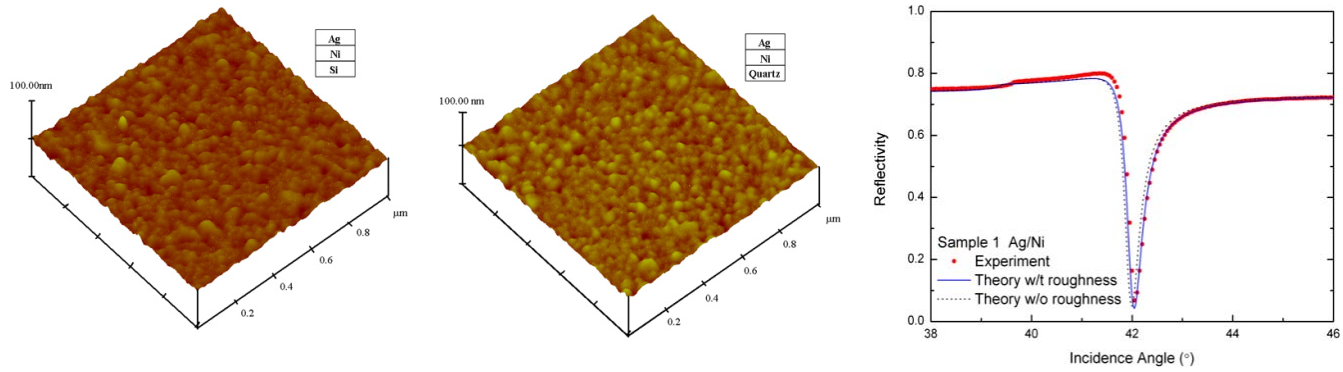

(a) (b) (c)

Fig. 20. AFM images of surface topographies of 50 nm Ag/2 nm Ni deposited on (a) silicon and (b) quartz respectively. (c) The surface plasmon resonance reflectivity curve.

roughness for the Ag film while at the same time maintaining and enhancing the plasmonic properties of the combined structures at 632.8 nm wavelength.

The effect of surface morphology on the optical properties in metal−dielectric−metal (MDM) thin film was also investigated by using a Ag/MgF_2/Ag system deposited on Si substrate with varied evaporation rate and thus different surface roughness and grain size.[90] The reflectance spectra of the Ag/MgF_2/Ag films show a dip due to surface roughness-induced excitation of surface plasmon polaritons. The dip position varies from 650 to 800 nm, depending on the surface morphology of the multi-layered film. Figure 21(a) shows the reflectance spectrum for samples at different deposition rate. The SPP excitation at the air/Ag interface due to the surface roughness is the main reason to cause the reflectance dip. The measured spectra are well matched with Fresnel reflection simulation of the multi-layer film by using the Drude−Lorentz function and Maxwell−Garnet theory for the discontinuous Ag film. We found that the filling ratio of the Ag film plays an important role in determining the dip position and the damping factor is the main contribution to the linewidth. Interesting empirical relations were also found between the optical properties and the morphology information, as showed in Fig. 21(b), where the dip position is proportional to filling factor f, surface roughness δ and the Ag grain size d, $\lambda \sim f\delta d^3$. The study is important to metal-dielectric-based structures for high resolution super-resolution imaging. The unique features of such an MDM film could also be used for color filters.

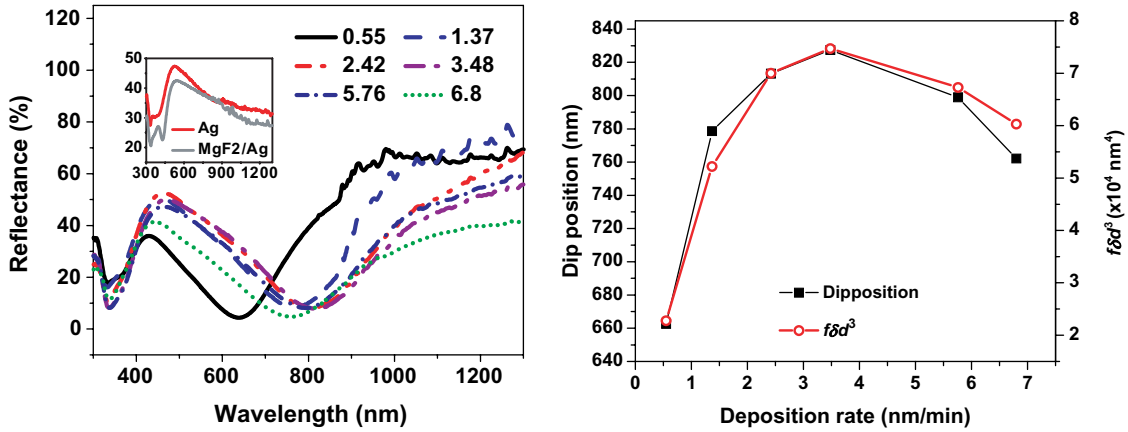

(a) (b)

Fig. 21. (a) Plot of different reflectance spectra for samples at different deposition rates. The inset shows the reflectance spectrum for a single Ag film and MgF_2/Ag film on Si substrate. (b) Correlation between the dip positions of reflectance spectra with film morphology properties.

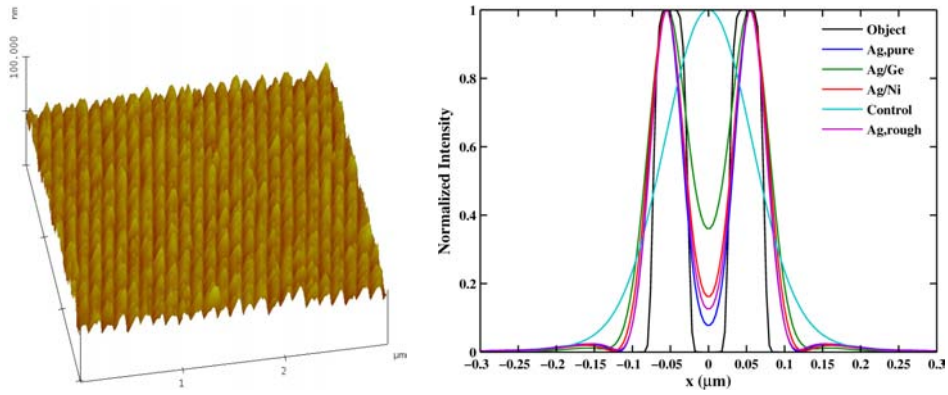

(a) (b)

Fig. 22. (a) Subdiffraction-limited optical images by superlens scanned by AFM. (b) Point spread function calculation of the superlens imaging effect for different Ag layers. All the films have the roughness counted. One more curve for pure Ag film without roughness and one control sample for no-Ag layer are also included.

Superlens by using a thin Ag film had been proved to be able to realize subdiffraction limitation imaging at near field. Image contrast and resolution are the key factors to evaluate superlens imaging ability. The subdiffraction-limited image is conventionally converted into the photoresist (PR) topographic modulations and then read by AFM scanning. We applied the Ag, Ag/Ni and Ag/Ge film to the superlens application by using a Cr grating with a linewidth of 55 nm and space of 45 nm as the object. A planarization process before the Ag film deposition was conducted and achieved a smoothness of less than 1 nm. The recorded optical images in PR were characterized by AFM in tapping mode. The depth obtained by scanning over the surface topography of the developed PR in the pure Ag superlens is larger than Ag/Ni superlens while the Ag/Ge lens has the least depth contrast.

Figure 22(a) shows a typical AFM three-dimensional picture of the developed PR after the Ag superlens imaging process; Fig. 22(b) shows the simulated point spread function for different Ag layer superlens. Both experimental and simulation results showed that the Ag superlens has the highest contrast compared to Ag/Ni and Ag/Ge superlens. The key reason could lie on the fact that all the Ag layers deposited on the smooth planarization polymer layer have no big difference in surface roughness and the role of seed layer in reducing surface roughness is not eminent in the superlens structure. Interestingly, the contrasts of all the three superlens are significantly higher than those in previous reports, where the scanned depth of PR profile varied from about only 5 to 10 nm or even less. The FWHM of the cross-section of the image PR line, which stands for the resolution of superlens, was measured at about 70 nm. It shows that this superlens is able to resolve a 45 nm-wide object by a near field imaging of about 70 nm FWHM.

In summary, the A*STAR Metamaterials Programme has made a number of interesting discoveries and technology innovations in metamaterials, plasmonics and super-resolution imaging.[112–131] These results should be helpful for the development of the metamaterials science and technology especially the superlens/hyperlens for future nanoscope technology. The team is continuing the efforts and will try to transform ideas, academic results and patents into real applications in industries for Singapore's economy growth.

7. Conclusion

In the past, scientists focused on the theoretical and experimental studies of metamaterial structures, be it in the microwave or optical range. After better understanding on the mechanism to form magnetic and double negative materials, the efforts has been moved to low-loss, three-dimensional, isotropic metamaterial in the visible range. The major interest for developing such structures is in the potential application of super-resolution imaging. Nevertheless, it remains a challenge to design and fabricate low-loss metamaterial structures with specific negative index over a certain wavelength range for imaging application. In addition, the realization of three-dimensional structures especially at small dimensions is a nontrivial work. With much interest and efforts worldwide, we foresee more breakthroughs

in metamaterials research and more metamaterials enabled applications in markets like optical nanoscope in the near future.

References

1. Veselago VG, The electrodynamics of substances with simultaneously negative values of ε and μ, *Sov Phys Usp* **10**:509, 1968.
2. Padilla WJ, Basov DN and Smith DR, Negative refractive index metamaterials, *Materials Today* **9**:28, 2006.
3. Pendry JB, Negative refraction makes a perfect lens, *Phys Rev Lett* **85**:3966, 2000.
4. Smith DR, Pendry JB and Wiltshire MCK, Metamaterials and negative refractive index, *Science* **305**:788−792, 2004.
5. Zhang X and Liu ZW, Superlenses to overcome the diffraction limit, *Nature Materials* **7**:435−441, 2008.
6. Pacheco J, Theory and application of left-handed metamaterials, PhD thesis, Massachusetts Institute of Technology, 2004.
7. Kong SC *et al.*, Band-stop filter based on a substrate embedded with metamaterials, *Microw Opt Tech Lett* **49**:530, 2007.
8. Landy NI *et al.*, Perfect metamaterial absorber, *Phys Rev Lett* **100**:207402, 2008.
9. Nefedov IS and Tretyakov SA, On potential applications of metamaterials for the design of broadband phase shifters, *Microw Opt Tech Lett* **45**:98, 2005.
10. Schurig D *et al.*, Metamaterial electromagnetic cloak at microwave frequencies, *Science* **314**:977, 2006.
11. Cai WS *et al.*, Optical cloaking with metamaterials, *Nat Photonics* **1**:224, 2007.
12. Salandrino A and Engheta N, Far-field subdiffraction optical microscopy using metamaterial crystals: Theory and simulations, *Phys Rev B* **74**:075103, 2006.
13. Smolyaninov II, A far-field optical microscope with nanometer-scale resolution based on in-plane surface plasmon imaging, *J Opt A: Pure Appl Opt* **7**:S165, 2005.
14. Abbe E, *Arch Mikroskop Anat* **9**:413−420, 1873.
15. Born M and Wolf E, *Principles of Optics*, 4th edn. Pergamon Press: New York, 1970.
16. Fang NH, Sun LC and Zhang X, Sub-diffraction-limited optical imaging with a silver superlens, *Science* **308**:534−537, 2005.
17. Liu ZW *et al.*, Far-field optical hyperlens magnifying sub-diffraction-limited objects, *Science* **315**:1686, 2007.
18. Li JS *et al.*, Experimental demonstration of an acoustic magnifying hyperlens, *Nature Materials* **8**:931−934, 2009.
19. Pendry JB *et al.*, Extremely low frequency plasmons in metallic mesostructures, *Phys Rev Lett* **76**(25):4773−4776, 1996.
20. Pendry JB, Martin-Moreno L and Garcia-Vidal FJ, Mimicking surface plasmons with structured surfaces, *Science* **305**:847−848, 2004.
21. Garcia-Vidal FJ, Martin-Moreno L and Pendry JB, Surfaces with holes in them: New plasmonic metamaterials, *J Opt A: Pure Appl Opt* **7**:S97−S101, 2005.
22. Hibbins AP, Evans BR and Sambles JR, Experimental verification of designer surface plasmons, *Science* **308**:670−672, 2005.
23. Pendry JB *et al.*, Magnetism from conductors and enhanced nonlinear phenomena, *IEEE Trans Microwave Theory Tech* **47**:2075−2084, 1999.
24. Smith DR *et al.*, Composite medium with simultaneously negative permeability and permittivity, *Phys Rev Lett*, **84**:4184−4187, 2000.
25. Shelby RA *et al.*, Microwave transmission through a two-dimensional, isotropic, left-handed metamaterial, *Appl Phys Lett* **78**(4): 489−491, 2001.
26. Shelby RA, Smith DR and Schultz S, Experimental verification of a negative index of refraction, *Science* **292**:77, 2001.
27. Quan BG *et al.*, Time-resolved broadband analysis of split ring resonators in terahertz region, *Appl Phys Lett* **89**:041101, 2006.
28. Yen TJ *et al.*, Terahertz magnetic response from artificial materials, *Science* **303**:1494−1496, 2004.
29. Zhang S *et al.*, Midinfrared resonant magnetic nanostructures exhibiting a negative permeability, *Phys Rev Lett* **94**:037402, 2005.
30. Linden S *et al.*, Magnetic response of metamaterials at 100 Terahertz, *Science* **306**:1351−1353, 2004.
31. Enkrich C *et al.*, Magnetic metamaterials at telecommunication and visible frequencies, *Phys Rev Lett* **95**:203901, 2005.
32. Klein MW *et al.*, Second-harmonic generation from magnetic metamaterials, *Science* **313**:502−504, 2006.
33. Dolling G *et al.*, Cut-wire pairs and plate pairs as magnetic atoms for optical metamaterials, *Opt Lett* **30**:3198−3200, 2005.
34. Zhang S *et al.*, Experimental demonstration of near-infrared negative-index metamaterials, *Phys Rev Lett* **95**:137404, 2005.
35. Zhang S *et al.*, Near-infrared double negative metamaterials, *Opt Exp* **13**:4922−4930, 2005.
36. Zhang S *et al.*, Demonstration of metal-dielectric negative metamaterials with improved performance at optical frequencies, *J Opt Soc Am B* **23**:434−438, 2006.

37. Dolling G *et al.*, Low-loss negative-index metamaterial at telecommunication wavelengths, *Opt Lett* **31**:1800−1802, 2006.
38. Dolling G *et al.*, Negative-index metamaterials at 780 nm wavelength, *Opt Lett* **32**:53−55, 2007.
39. Wu W *et al.*, Geometrical dependence of optical negative index meta-materials at 1.55 μm, *Appl Phys A* **95**:1119−1122, 2009.
40. Chettiar UK *et al.*, Dual-band negative index metamaterial: double negative at 813 nm and single negative at 772 nm, *Opt Lett* **32**:1671−1673, 2007.
41. Cai WS *et al.*, Metamagnetics with rainbow colors, *Opt Express* **15**:3333−3341, 2007.
42. SM Xiao *et al.*, Yellow-light negative-index metamaterials, *Opt Lett* **34**:3478−3480, 2009.
43. Chettiar UK *et al.*, Negative index metamaterial combining magnetic resonators with metal films, *Opt Express* **14**:7872−7877, 2006.
44. Ku Z and Brueck SRJ, Comparison of negative refractive index materials with circular, elliptical and rectangular holes, *Opt Express* **15**:4515−4522, 2007.
45. Dolling G *et al.*, Design-related losses of double-fishnet negative-index photonic metamaterials, *Opt Express* **15**:11536−11541, 2007.
46. Zhou JF, Koschny T and Soukoulis CM, An efficient way to reduce losses of left-handed metamaterials, *Opt Express* **16**:11147−11152, 2008.
47. Ding P *et al.*, Influence of metal-layer thickness on the losses in fishnet metamaterial, 2008 International workshop on metamaterials (IEEE Press, 2008), pp. 191−193.
48. Minovich A *et al.*, Influence of the substrate on negative index fishnet metamaterials, *Opt Comm* **283**:4770−4774, 2010.
49. Yan CC *et al.*, Negative refractive indices of a confined discrete fishnet metamaterial at visible wavelengths, *J Opt Soc Am B* **25**:1815−1819, 2008.
50. Kwon DH *et al.*, Near-infrared metamaterials with dual-band negative-index characteristics, *Opt Express* **15**:1647−1652, 2007.
51. Boardman AD *et al.*, Active and tunable metamaterials, **5**:287−307, 2011.
52. Liu N *et al.*, *Nat Photonics* **3**:157−162, 2009.
53. Minovich A *et al.*, Tunable fishnet metamaterials infiltrated by liquid crystals, *Appl Phys Lett* **96**:193103, 2010.
54. Xiao SM *et al.*, Tunable magnetic response of metamaterials, *Appl Phys Lett* **95**:033115, 2009,
55. Werner DH *et al.*, Liquid crystal clad near-infrared metamaterials with tunable negative-zero-positive refractive indices, *Opt Express* **15**:3342−3347, 2007.
56. Ponizovskaya EV and Bratkovsky AM, Metallic negative index nanostructures at optical frequencies: Losses and effect of gain medium, *Appl Phys A* **87**:161−165, 2007.
57. Wuestner S *et al.*, Overcoming losses with gain in a negative refractive index metamaterial, *Phys Rev Lett* **107**:127401, 2010.
58. Sarychev AK and Tartakovsky G, Magnetic plasmonic metamaterials in actively pumped host medium and plasmonic nanolaser, *Phys Rev B* **75**:085436, 2007.
59. Klar TA *et al.*, Negative index metamaterials: Going optical, *IEEE J Sel Top Quant Electron* **12**:1106−1115, 2006.
60. Ramakrishna SA and Pendry JB, Removal of absorption and increase in resolution in a near-field lens via optical gain, *Phys Rev B* **67**:201101, 2003.
61. Xiao SM *et al.*, Loss-free and active optical negative-index metamaterials, *Nature* **466**:735−740, 2010.
62. Zhang S *et al.*, Optical negative-index bulk metamaterials consisting of 2D perforated metal-dielectric stacks, *Opt Express* **14**:6778−6787, 2006.
63. Dolling G, Wegener M and Linden S, Realization of a three-functional-layer negative-index photonic metamaterial, *Opt Lett* **32**:551−553, 2007.
64. Boltasseva A and Shalaev VM, Fabrication of optical negative-index metamaterials: Recent advances and outlook, *Metamaterials* **2**:1−17, 2008.
65. Liu N *et al.*, Three-dimensional photonic metamaterials at optical frequencies, *Nat Mater* **7**:31−37, 2008.
66. Liu N *et al.*, Plasmonic building blocks for magnetic molecules in three-dimensional optical metamaterials, *Adv Mater* **20**:3859−3865, 2008.
67. Bergmair I *et al.*, 3D materials made of gold using nanoimprint lithography, *Microelect Eng* **87**:1008−1010, 2010.
68. Valentine J *et al.*, Three-dimensional optical metamaterial with a negative refractive index, *Nature* **455**:376−380, 2008.
69. Garcia-Meca C *et al.*, Low-loss multilayered metamaterial exhibiting a negative index of refraction at visible wavelengths, *Phys Rev Lett* **106**:067402, 2011.
70. Padilla WJ, Smith DR and Basov DN, Spectroscopy of metamaterials from infrared to optical frequencies, *J Opt Soc Am B* **23**:(3) 404−414, 2006.
71. Shalaev VM, Optical negative-index metamaterials, *Nature Photonics* **1**:41−48, 2007.
72. Soukoulis CM and Wegener M, Optical metamaterials-more bulky and less 'lossy', *Science* **330**:1633−1634, 2010.
73. Pendry JB, Negative refraction, *Contemp Phys* **45**:191−202, 2004.
74. Ramakrishna SA *et al.*, Imaging the near field, *J Mod Opt* **50**:1419−1430, 2003.

75. David OSM and Richard JB, Super-resolution imaging through a planar silver layer, *Opt Express* **13**:2127−2134, 2005.
76. Alina S *et al.*, A superlens for the deep ultraviolet, *Appl Phys Lett* **95**:121909, 2009.
77. Zhong S, Vladimir K and Fei W, 193 nm superlens imaging structure for 20 nm lithography node, *Opt Express* **17**:11309−11314, 2009.
78. Jeppesen C *et al.*, Thin film Ag superlens towards lab-on-a-chip integration, *Opt Express* **17**:22543−22552, 2009.
79. Pratik C *et al.*, A smooth optical superlens, *Appl Phys Lett* **96**:043102, 2010.
80. Taubner T *et al.*, Near-field microscopy through a SiC superlens, *Science* **313**:1595, 2006.
81. Stephane D *et al.*, Theory of the transmission properties of an optical far-field superlens for imaging beyond the diffraction limit, *J Opt Soc Am B* **23**:2383−2392, 2006.
82. Liu ZW *et al.*, Far-field optical superlens, *Nano Lett* **7**:403−408, 2007.
83. Lee H *et al.*, Design, fabrication and characterization of a far-field superlens, *Solid State Commun.* **146**:202−207, 2008
84. Wood B, Pendry JB and Tsai DP, Directed subwavelength imaging using a layered metal-dielectric system, *Phys Rev B* **74**:115116, 2006.
85. Scalora M *et al.*, Negative refraction and subwavelength focusing in the visible range using transparent metallo-dielectric stacks, *Opt Express* **15**:508−523, 2007.
86. Mattiucci N *et al.*, Transmission function properties for multi-layered structures: Application to super-resolution, *Opt Express* **17**:17517−17528, 2009.
87. Bloemer MJ *et al.*, Energy considerations for a superlens based on metal/dielectric multilayers, *Opt Express* **16**:19342−19353, 2008.
88. Nielsen RB *et al.*, Toward superlensing with metal-dielectric composites and multilayers, *Appl Phys B* **100**:93−100, 2010.
89. Chen W *et al.*, Fabrication and optical characterizations of smooth silver-silica nanocomposite films, *Laser Phys Lett* **7**:677−684, 2010.
90. Leong ESP *et al.*, Effect of surface morphology on the optical properties in metal-dielectric-metal thin film systems, *ACS Appl Mater Interfaces*, in press, doi: 10.1021/am101278q.
91. Jacob Z, Alekseyev L and Narimanov E, Optical hyperlens: Far-field imaging beyond the diffraction limit, *Opt Express* **14**:8247−8256, 2006.
92. Smith DR and Schurig D, Electromagnetic wave propagation in media with indefinite permittivity and permeability tensors, *Phys Rev Lett* **90**:077405, 2003.
93. Ma C, Aguinaldo R and Liu Z, Advances in the hyperlens, *Chin Sci Bull* **24**:2618−2624, 2010.
94. Jacob Z, Alekseyev L and Narimanov E, Semiclassical theory of the hyperlens, *J Opt Soc Am A* **24**:A52−A59, 2007.
95. Kildishev A and Narimanov E, Impedance-matched hyperlens, *Opt Lett* **32**:3432−3434, 2007.
96. Liu ZW *et al.*, Far-field optical hyperlens magnifying sub-diffraction-limited objects, *Science* **315**:1686, 2007.
97. Smolyaninov II, Hung Y and Davis CC, Magnifying superlens in the visible frequency range, *Science* **315**:1699−1701, 2007.
98. Smolyaninov II *et al.*, Far-field optical microscopy with a nanometer-scale resolution based on the in-plane image magnification by surface plasmon polaritons, *Phys Rev Lett* **94**:057401, 2005.
99. Smith EJ *et al.*, System investigation of a rolled-up metamaterial optical hyperlens structure, *Appl Phys Lett* **95**:083104, 2009.
100. Smith EJ *et al.*, Erratum: System investigation of a rolled-up metamaterial optical hyperlens structure, *Appl Phys Lett* **96**:019902, 2010.
101. Rho J *et al.*, Spherical hyperlens for two-dimensional sub-diffractional imaging at visible frequencies, *Nature Commun* **1**:143, 2010.
102. Johnson PB and Christy RW, Optical constants of the noble metals, *Phys Rev B* **6**:4370, 1972.
103. Xiong Y, Liu ZW and Zhang X, A simple design of flat hyperlens for lithography and imaging with half-pitch resolution down to 20 nm, *Appl Phys Lett* **94**:203108, 2009.
104. Schwaiger S *et al.*, Rolled-up three-dimensional metamaterials with a tunable plasma frequency in the visible regime, *Phys Rev Lett* **102**:163903, 2009.
105. Gibbons N *et al.*, Scalable cylindrical metallodielectric metamaterials, *Adv Mater* **21**:3933−3936, 2009.
106. Burckel DB *et al.*, Fabrication of 3D metamaterial resonators using self-aligned membrane projection lithography, *Adv Mater* **22**:3173−3175, 2010.
107. Burckel DB *et al.*, Micrometer-scale cubic unit cell 3D metamaterial layers, *Adv Mater* **22**:5053−5057, 2010.
108. Casse BDF *et al.*, Super-resolution imaging using a three-dimensional metamaterials nanolens, *Appl Phys Lett* **96**:023114, 2010.
109. Liu ZW *et al.*, Far-field optical superlens, *Nano Lett* **7**:403−408, 2007.
110. Lee H *et al.*, Design, fabrication and characterization of a far-field superlens, *Solid State Comm* **146**:202−207, 2008.
111. Liu H *et al.*, Enhanced surface plasmon resoance on a smooth silver film with a seed growth layer, *ACS Nano* **4**:3139−3146, 2010.

112. Zhu S *et al.*, Fully complementary metal-oxide-semiconductor compatible nanoplasmonic slot waveguides for silicon electronic photonic integrated circuits, *Appl Phys Lett* **98**:021107 2011.
113. Ren FF *et al.*, Split bull's eye shaped aluminum antenna for plasmon-enhanced nanometer scale germanium photodetector, *Nano Lett* **11**:1289, 2011.
114. Zhu S, Lo G and Kwong D, Theoretical investigation of silicon MOS-type plasmonic slot waveguide based MZI modulators, *Opt Express* **18**:27802, 2010.
115. Zhang DG, Yuan XC and Teng JH, Surface plasmon-coupled emission on metallic film coated with dye-doped polymer nano-gratings, *Appl Phys Lett* **97**:231117, 2010.
116. Yan C *et al.*, Metal-dielectric composites for beam splitting and far-field deep sub-wavelength resolution for visible wavelengths, *Opt Express* **18**:14794, 2010.
117. Yan C *et al.*, Dual refractions in metal nanorod-based metamaterials, *J Opt* **12**:065102, 2010.
118. Yan C, Li D and Zhang DH, Wedge-shaped metal-dielectric composite metamaterials for light control, *Metamaterials* **4**:170, 2010.
119. Wang Q *et al.*, Deterministic relief dielectric structures to realize phase modulation of surface-plasmon polaritons, *Opt Lett* **35**:4196, 2010.
120. Szabo Z *et al.*, A unique extraction of metamaterial parameters based on Kramers−Kronig relationship, *IEEE Tran MTT* **58**:2646, 2010.
121. Ren FF *et al.*, Surface plasmon enhanced responsivity in a waveguided germanium metal-semiconductor-metal photodetector, *Appl Phys Lett* **97**:091102, 2010.
122. Luk'yanchuk B *et al.*, The fano resonance in plasmonic nanostructures and metamaterials, *Nat Mat* **9**:707, 2010.
123. Ewe WB *et al.*, Field enhancement of gold optical nanoantennas mounted on a dielectric waveguide, *Appl Phys A* **100**:315, 2010.
124. Evlyukhin AB *et al.*, Optical response features of Si-nanoparticle arrays, *Phys Rev B* **82**:45404, 2010.
125. Chu HS *et al.*, Optical performance of single-mode hybrid dielectric-loaded plasmonic waveguide-based components, *Appl Phys Lett* **96**:221103, 2010.
126. Chu HS *et al.*, Field enhancement by semi-nano-capsule plasmonic antenna at the visible violet wavelength, *Appl Phys A* **100**:353, 2010.
127. Zhu WM *et al.*, Switchable magnetic metamaterials using micromachining processes, *Adv Mater* **23**:1792−1796, 2011.
128. Zhang L *et al.*, Design and fabrication of sub-wavelength nanograting based light emitting diode, *Appl Phys A*, 2011, doi: 10.1007/s00339-011-6295-2.
129. Yan CC *et al.*, Spherical metallic nanoparticle arrays for super-resolution imaging, *J Appl Phys* **109**:063105, 2011.
130. Wang Z *et al.*, Optical virtual imaging at 50 nm lateral resolution with a white-light nanoscope, *Nat Commun* **2**, 2011, doi:10.1038/ncomms1211.
131. Rahmani M *et al.*, Generation of pronounced fano resonances and tuning of subwavelength spatial light distribution in plasmonic pentamers, *Opt Exp* **19**:063105, 2011.